C. R. Physique 20 (2019) 569–582

Contents lists available at ScienceDirect

Comptes Rendus Physique

www.sciencedirect.com

Studies on the cold binary fragmentation of even–even $^{230–250}$U isotopes

Étude de la fragmentation froide binaire des isotopes pairs–pairs $^{230–250}$U

Kolathu Parambil Santhosh *, Annu Cyriac

School of Pure and Applied Physics, Kannur University, Swami Anandatheertha Campus, Payyanur 670327, Kerala, India

ARTICLE INFO

Article history:
Available online 25 March 2019

Keywords:
Heavy particle radioactivity
Spontaneous fission
Cold binary fission

Mots-clés :
Radioactivité des particules lourdes
Fission spontané
Fission froide binaire

ABSTRACT

Within the framework of the Coulomb and proximity potential model (CPPM), we studied the cold binary fission of even–even $^{230–250}$U isotopes using the two versions of the nuclear proximity potential, Proximity 1977 and Proximity 2000. The most favorable binary fission path is the one that has a high Q value and a minimum driving potential with respect to the mass and charge asymmetries. A nucleus with doubly-closed shell or near doubly-closed shell always appears as the heaviest nucleus in the favored channel of the binary fission of all the mentioned isotopes. For the ^{230,232,234}U isotopes, the highest yield was predicted for the isotope of Pb ($Z = 82$) as one fragment, whereas for the ^{236}U isotope, fragmentation with the isotope of Hg ($Z = 80$) as one fragment possesses the highest yield. For the ^{238}U isotope, fragmentation with the isotope of Pt ($Z = 78$, $N = 126$) as one fragment possesses the highest yield. In the case of the ^{240,242,244,246,248,250}U isotopes, the highest yield is for the fragmentation with Sn ($Z = 50$) as one fragment. It was found that asymmetric splitting is superior for U isotopes with mass number $A \leq 238$ and symmetric splitting is superior for U isotopes with $A \geq 240$. The computed penetrability and half-lives using the two different proximity potentials for the cold binary fission of $^{230–250}$U isotopes were compared with the available experimental data collected from Holden et al. [Pure Appl. Chem. 72 (2000) 1525]. The two results were found to be in agreement with each other.

RÉSUMÉ

Dans le cadre du modèle CPPM (Coulomb et potentiel de proximité), nous avons étudié la fission froide binaire d'isotopes pairs–pairs $^{230–250}$U, en utilisant les deux versions Proximity 1977 et Proximity 2000 du potentiel de proximité nucléaire. La voie la plus favorable pour la fission binaire est celle qui a une valeur de Q élevée et un potentiel d'entraînement minimal par rapport aux asymétries de masse et de charge. Pour tous les isotopes mentionnés, le canal le plus favorable est celui dans lequel le noyau le plus lourd est à couche doublement complète ou presque doublement complète. Pour les isotopes ^{230,232,234}U, on prévoit que le rendement le plus élevé est obtenu quand l'un des fragments est un isotope de Pb ($Z = 82$), tandis que, pour l'isotope ^{236}U, la fragmentation qui donne

* Corresponding author.
E-mail address: drkpsanthosh@gmail.com (K.P. Santhosh).

https://doi.org/10.1016/j.crhy.2018.11.009

naissance à un isotope du mercure ($Z = 80$) a le meilleur rendement. Pour l'isotope ^{238}U, la fragmentation conduisant à l'isotope de platine ($Z = 78$, $N = 126$) a le rendement le plus élevé. Dans le cas des isotopes ^{240,242,242,244,244,246,248,250}U, le rendement le plus élevé est obtenu quand la fragmentation mène à l'étain ($Z = 50$). Le fractionnement asymétrique est favorisé pour les isotopes de l'uranium avec un nombre de masse $A \leq 238$ et le fractionnement symétrique pour les isotopes de l'uranium avec $A \geq 240$. La pénétrabilité et les demi-vies calculées à l'aide des deux potentiels de proximité pour la fission froide binaire des isotopes $^{230–250}$U ont été comparées aux données expérimentales disponibles, reproduites par Holden et al. (Pure Appl. Chem. 72 (2000) 1525). On a constaté que les deux résultats étaient en bon accord.

1. Introduction

Pioneering studies on nuclear fission have played a key role in understanding the nuclear phenomena and related properties. The low-energy fission of heavy elements ($Z > 90$) was one of the most complex phenomena of nuclear reactions. Most of the nuclear reactions take place through the binary fission process, a low-energy fission, where the fissioning nucleus ends up in two fission fragments and the fragments were formed after overcoming the fission barrier. In 1939, Hahn et al. [1] discovered that the uranium atom was fragmented into two parts, which are more or less equal in size. Bohr and Wheeler [2] developed a theory of fission based on the liquid drop model. The authors gave a theory of the effect based on the usual ideas of penetration of potential barriers. Milton et al. [3] noticed that during fission, some of the fragments are produced at high kinetic energies, whereby emerging nuclei are formed nearly in their ground state. As a consequence, fragments will not possess excitation energy and neutrons will not be emitted. In order to achieve such large kinetic energy values, the scission point configurations should correspond to very compact shapes and consequently the deformations for final fragments are close to that of their ground states [4,5]. This kind of nuclear fission is termed cold fission or neutronless fission. Guet et al. [6], determined the mass distributions of the primary fragments for the highest values of the kinetic energy, and concluded that the superposition of two fragments takes place in their ground state even before scission, from which the cold fragmentation term emerged. The cold (neutronless) fission of many actinide nuclei leading to fragments with masses of approximately 70–160 atomic mass units has also been studied [4,7–13]. Montoyo et al. [14] studied even–odd effects of the minimal total fragmentation excitation energy in the thermal neutron-induced fission of ^{233}U and ^{235}U as well as the spontaneous fission of ^{252}Cf. Asghar et al. [15] used the "Cosi fan tutte" spectrometer installed at the high-flux reactor of the "Institut Laue-Langevin", Grenoble, France, to measure the light-fragment-group mass–energy correlations for ^{229}Th(n_{th}, f), ^{232}U(n_{th}, f), and ^{239}Pu(n_{th}, f) and found that the shells in the nascent fragments seem to play an important role in the thermal-neutron-induced fission. Within the Hartree–Fock–Bogoliubov (HFB) [16–18] framework, based on the highly predictive parametrizations, DIM [19], DIS [20], and DIN [21] of the Gogny [22] Energy-Density Functional (EDF), Rodriguez et al. [23] described the fission in the isotopes $^{232–280}$U and computed the fission paths, collective masses, and zero-point quantum corrections.

In the present paper, we have considered even–even uranium isotopes with the mass numbers $A = 230$, 232, 234, 236, 238, 240, 242, 244, 246, 248, and 250, and estimated the yield in the binary fragmentation of these isotopes using two versions of the nuclear proximity potential, Proximity 1977 and Proximity 2000, by minimizing the fragmentation potential with respect to the mass and charge asymmetries. Shi and Swiatecki [24] used the proximity potential for the first time in an empirical manner to study asymmetric fission, and Gupta et al. [25] used it extensively in the preformed cluster model (PCM). Myers et al. [26] and Reisdorf [27] suggested several modifications over the real proximity potential. Dutt et al. [28–30] have used the proximity potential of different versions for studies involving the fusion cross section of different target–projectile combinations. Yao et al. [31] used different proximity potentials to calculate the half-lives of the alpha decay for even–even nuclei from light to heavy mass. The proximity potential has been used broadly for studies in the areas of alpha decay [32–35], cluster decay [36–39], ternary fission [40–42], alpha decay of heavy and superheavy nuclei [43–45] and cluster radioactivity of superheavy nuclei [44]. In the present work, which is an extension of our earlier work [46], we have computed the penetrability and half-lives using the two different proximity potentials for the cold binary fission of $^{230–250}$U isotopes, which were compared with the available experimental data collected from Holden et al. [47]. We would like to mention that a similar study has been performed on even–even $^{244–258}$Cf isotopes and even–even $^{238–248}$Pu isotopes by Santhosh et al. [48,49], where the cold reaction valleys were plotted, and the corresponding barrier penetrability and yields were calculated for all binary fragmentations of the above-mentioned isotopes.

The methodology employed for our calculation is described in Section 2. The details of the study can be found in Section 3, results and discussion. The conclusions are summarized in Section 4.

2. The model

If the value of Q of the reaction is positive, the binary fission is energetically possible, i.e.

$$Q = M - \sum_{i=1}^{2} m_i > 0 \tag{1}$$

Here M is the mass excess of the parent, m_i is the mass excess of the fragments. A parent nucleus exhibiting binary fission has the interacting potential V given by

$$V = \frac{Z_1 Z_2 e^2}{r} + V_{\mathrm{p}}(z) + \frac{\hbar^2 \ell(\ell+1)}{2\mu r^2}, \quad \text{for } z > 0 \tag{2}$$

Here Z_1 and Z_2 are the atomic numbers of the fission fragments, z is the distance between the near surfaces of the two fragments, r is the distance between the centers of these fragments and is given as $r = z + C_1 + C_2$, where C_1 and C_2 are the Süsmann central radii of fragments. The term ℓ represents the angular momentum, μ the reduced mass and V_{p} is the proximity potential. The proximity potential V_{p} is given by Blocki et al. [50] as

$$V_{\mathrm{p}}(z) = 4\pi\gamma b \left[\frac{C_1 C_2}{(C_1 + C_2)}\right] \Phi\left(\frac{z}{b}\right) \tag{3}$$

where γ is the nuclear surface tension coefficient and Φ represents the universal proximity potential [51].

2.1. Proximity potential 1977

The nuclear surface tension coefficient γ is given by,

$$\gamma = 0.9517\left[1 - 1.7826(N-Z)^2/A^2\right] \mathrm{MeV/fm^2} \tag{4}$$

where N, Z, and A represents neutron, proton and mass number of the parent, respectively, Φ represents the universal proximity potential [51] given as

$$\Phi(\xi) = -4.41 \mathrm{e}^{-\xi/0.7176}, \quad \text{for } \xi > 1.9475, \tag{5}$$

$$\Phi(\xi) = -1.7817 + 0.9270\xi + 0.0169\xi^2 - 0.05148\xi^3, \quad \text{for } 0 \le \xi \le 1.9475 \tag{6}$$

with $\xi = z/b$, where the width (diffuseness) of the nuclear surface is $b \approx 1$ fm and the Süsmann central radii C_i of the fragments related to the sharp radii R_i are

$$C_i = R_i - \left(\frac{b^2}{R_i}\right) \tag{7}$$

For R_i, we use the semi empirical formula in terms of mass number A_i as [50]

$$R_i = 1.28A_i^{1/3} - 0.76 + 0.8A_i^{-1/3} \tag{8}$$

2.2. Proximity potential 2000

There was a disagreement in the scientific community with regard to the barrier height as determined by Proximity 1977 and the experimental data [26]. Myers and Swiatecki [26] applied recent data for nuclear radii and surface tension coefficients and developed the novel droplet model. Using this droplet model [52], the matter radius C_i was calculated as:

$$C_i = c_i + \frac{N_i}{A_i} t_i \quad (i = 1, 2) \tag{9}$$

where c_i denotes the half-density radii of the charge distribution and t_i is the neutron skin of the nucleus. The nuclear charge radius (denoted as R_{00} in Ref. [53]) is given by the relation:

$$R_{00i} = \sqrt{5/3}\langle r^2\rangle^{1/2} \tag{10}$$

$$= 1.240A_i^{1/3}\left\{1 + \frac{1.646}{A_i} - 0.191\left(\frac{A_i - 2Z_i}{A_i}\right)\right\} \mathrm{fm} \quad (i = 1, 2) \tag{11}$$

where $\langle r^2\rangle$ represents the mean-square nuclear charge radius. According to Ref. [53], Eq. (10) was valid for the even–even nuclei with $8 \le Z < 38$ only. For nuclei with $Z \ge 38$, the above equation was modified by Pomorski et al. [53] as

$$R_{00i} = 1.256A_i^{1/3}\left\{1 - 0.202\left(\frac{A_i - 2Z_i}{A_i}\right)\right\} \text{ fm} \quad (i = 1, 2) \tag{12}$$

These expressions give a good estimate of the measured mean square nuclear charge radius $\langle r^2 \rangle$. The half-density radius c_i was obtained from the relation

$$c_i = R_{00i}\left(1 - \frac{7}{2}\frac{b^2}{R_{00i}^2} - \frac{49}{8}\frac{b^4}{R_{00i}^4} + \cdots\right) \quad (i = 1, 2) \tag{13}$$

Using the droplet model [50], the neutron skin t_i reads as

$$t_i = \frac{3}{2}r_0\left(\frac{JI_i - \frac{1}{12}c_1 Z_i A_i^{-1/3}}{Q + \frac{9}{4}JA_i^{-1/3}}\right) \quad (i = 1, 2) \tag{14}$$

Here r_0 is 1.14 fm, the value of the nuclear symmetric energy coefficient is $J = 32.65$ MeV, and $c_1 = 3e_2/5r_0 = 0.757895$ MeV. The neutron skin stiffness coefficient Q was taken to be 35.4 MeV. The nuclear surface energy coefficient γ in terms of neutron skin was given as

$$\gamma = \frac{1}{4\pi r_0^2}\left[18.63 \text{ (MeV)} - Q\,\frac{(t_1^2 + t_2^2)}{2r_0^2}\right] \tag{15}$$

where t_1 and t_2 were calculated using Eq. (13). The universal function $\Phi(\xi)$ was reported as

$$\Phi(\xi) = \left\{-0.1353 + \sum_{n=0}^{5}\left[\frac{c_n}{n+1}\right](2.5 - \xi)^{n+1}\right\} \quad \text{for } 0 < \xi \le 2.5 \tag{16}$$

$$\Phi(\xi) = -0.09551\exp\left[(2.75 - \xi)/0.7176\right] \quad \text{for } \xi \ge 2.5 \tag{17}$$

The values of different constants c_n were $c_0 = -0.1886$, $c_1 = -0.2628$, $c_2 = -0.15216$, $c_3 = -0.04562$, $c_4 = 0.069136$, and $c_5 = -0.011454$. For $\xi > 2.74$, the above exponential expression is the exact representation of the Thomas–Fermi extension of the proximity potential. This potential is labeled as Proximity 2000.

The potential for the internal part (overlap region) of the barrier is given by

$$V = a_0(L - L_0)^n, \quad \text{for } z < 0 \tag{18}$$

Here $L = z + 2C_1 + 2C_2$ and $L_0 = 2C$, the diameter of the parent nuclei. By the smooth matching of the two potentials at the touching point, it is possible to determine the constants a_0 and n.

Using the one-dimensional WKB approximation, the barrier penetrability P is given by

$$P = \exp\left\{-\frac{2}{\hbar}\int_a^b \sqrt{2\mu(V - Q)}\,\mathrm{d}z\right\} \tag{19}$$

The reduced mass μ is given as $\mu = mA_1A_2/A$, where m is the nucleon mass and A_1, A_2 are the mass numbers of the binary fission fragments, respectively. The turning points a and b are determined from the equation $V(a) = V(b) = Q$.

The ratio between the penetration probabilities of a given fragmentation over the sum of the penetration probabilities of all possible fragmentation is calculated as the relative yield and is given by

$$Y(A_i, Z_i) = \frac{P(A_i, Z_i)}{\sum P(A_i, Z_i)} \tag{20}$$

3. Results and discussion

We identified the probable fragments from the binary fission of even–even $^{230\text{–}250}$U isotopes through the cold reaction valley plots. The introduction of the cold reaction valley is related to the structure of minima in the driving potential. The driving potential is the difference between the interaction potential V and the decay energy Q of the reaction. The interaction potential is taken as the sum of the Coulomb and proximity potentials. The barrier penetrability is very sensitive to the Q value and is computed using the latest experimental mass tables of Wang et al. [54] wherever possible. When the experimental mass excess values were not available, we have calculated the Q values using the mass tables of KTUY [55].

The driving potential of all possible fragment channels (A_1, A_2) are calculated, and then a single pair of charges for each channel is determined by minimizing the driving potential with respect to η_Z, for a fixed value of η. We based our study on the mass asymmetry η and the charge asymmetry η_Z between the two heavy fragments, the relative separation between the different fragments, and the Q-value for the fission products. However, the predicted favorable channel for binary fission is the one characterized with high Q-value, which at the same time has a local minimum in the driving potential.

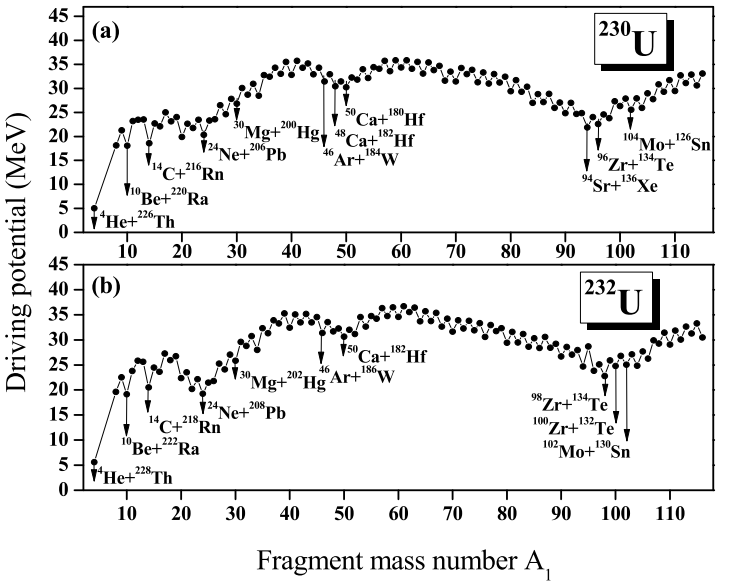

Fig. 1. Driving potential for the ^{230}U and ^{232}U isotopes, plotted as a function of the mass number A_1.

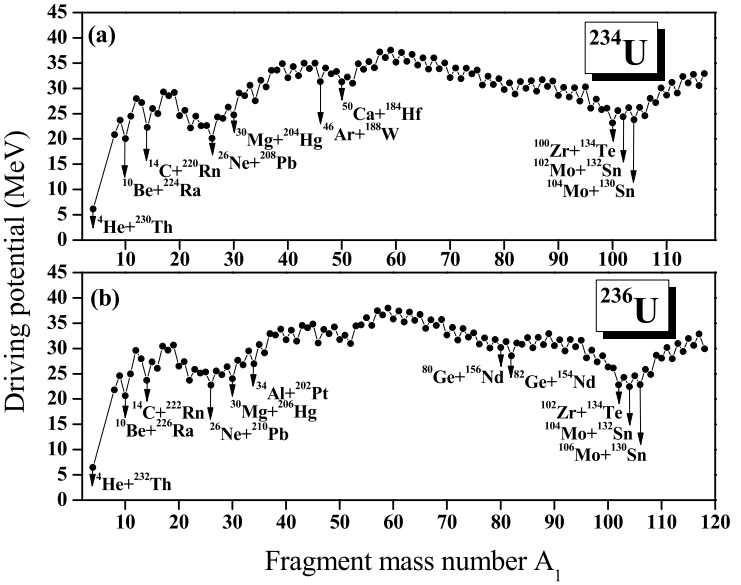

Fig. 2. Driving potential for the ^{234}U and ^{236}U isotopes, plotted as a function of the mass number A_1.

3.1. Cold reaction valley of even–even $^{230–250}$U isotopes

In the case of the binary fission of even–even $^{230–250}$U isotopes, its driving potentials for the touching configuration ($z = 0$) of fragment combinations are calculated. Figs. 1–6 represent the plots for the driving potential versus A_1 (mass of one fragment) for all the above isotopes. The observed mass-asymmetry valleys in these figures are because of the shell effects of one or both fragments. The fragment combinations having minima in the potential energy are the most probable binary fission fragments.

From Figs. 1–6, we noticed that, for ^{230}U apart from the alpha particle, ^{10}Be, ^{14}C, ^{20}O, ^{24}Ne, ^{28}Mg, ^{48,50}Ca,^{68,70}Ni, ^{94}Sr, ^{96}Zr, etc. are seen to be possible for emission, as these are the minima observed in the cold valley plot. Two deep regions are observed in the fission region, both having comparable minima. The minimum in the first region corresponds to the splitting ^{20}O + ^{210}Po and ^{24}Ne + ^{206}Pb, whereas that in the second region is due to the splitting ^{94}Sr + ^{136}Xe and ^{96}Zr + ^{134}Te. The driving potential values for the above combinations lie very close to each other. It was found that the four mentioned

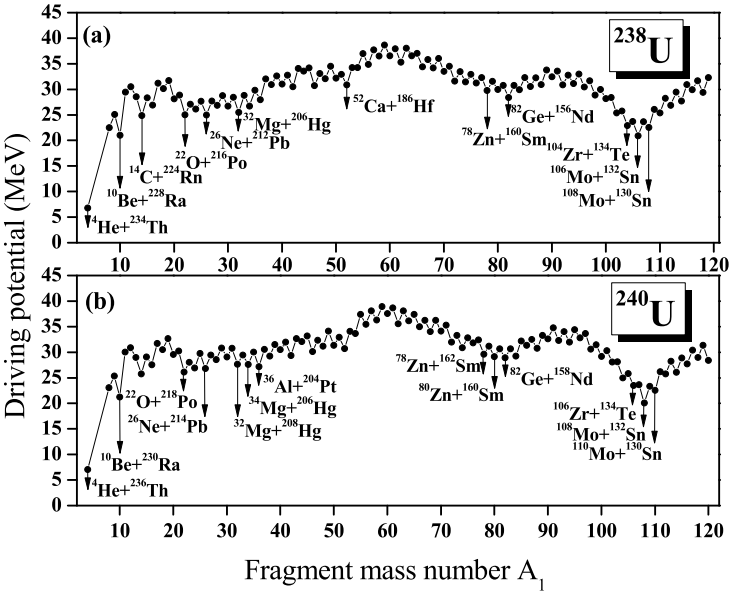

Fig. 3. Driving potential for the ^{238}U and ^{240}U isotopes, plotted as a function of the mass number A_1.

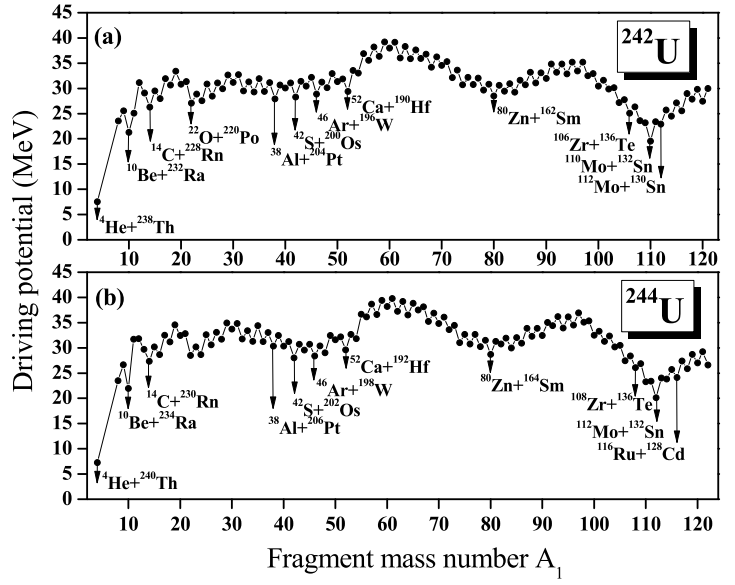

Fig. 4. Driving potential for the ^{242}U and ^{244}U isotopes, plotted as a function of the mass number A_1.

combinations include doubly or nearly doubly-magic nuclei viz, ^{210}Po ($N = 126$, $Z = 84$), ^{206}Pb ($N = 124$, $Z = 82$), ^{134}Te ($N = 82$, $Z = 52$) and ^{136}Xe ($N = 82$, $Z = 54$).

All the other isotopes also have deep valleys in the fission regions, each having several comparable minima. For the ^{232,234,236}U isotopes, the minima obtained in the first region are at ^{210,212,214}Po and ^{208,210}Pb, and they are due to the doubly-magic ^{208}Pb ($N = 126$, $Z = 82$), near doubly-magic ^{210}Po ($N = 126$, $Z = 84$), ^{212}Po ($N = 128$, $Z = 84$) and ^{210}Pb ($N = 128$, $Z = 82$). The minima observed in the second region are at ^{46}Ar ($N = 28$, $Z = 18$) and ^{50}Ca ($N = 30$, $Z = 20$). In the third region, minima are observed at ^{134}Te ($N = 82$, $Z = 52$) and ^{132}Sn ($N = 82$, $Z = 50$).

For the ^{238,240,242}U isotope, a deep minimum is observed at ^{106}Mo + ^{132}Sn, ^{108}Mo + ^{132}Sn and ^{110}Mo + ^{132}Sn respectively, due to the presence of doubly-magic ^{132}Sn. Other minima are observed at ^{52}Ca, ^{82}Ge, ^{206}Hg, ^{212}Pb, etc.

For ^{244,246,248,250}U, three distinguishable deep valleys are observed in the cold valley plot. It can be seen that, in the first region, minima are observed at ^{202}Os ($N = 126$), ^{198}W ($N = 124$), ^{200}W ($N = 126$) and ^{198}Hf ($N = 126$). In the second region, the observed minima are at ^{84}Ge ($N = 52$), ^{78}Ni ($N = 50$) and ^{80}Zn ($N = 50$). Finally, in the third valley, a minimum

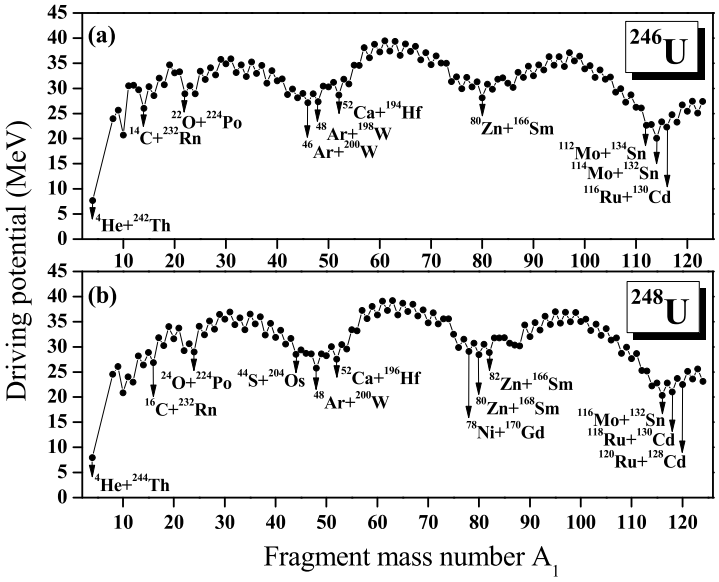

Fig. 5. Driving potential for the ^{246}U and ^{248}U isotopes, plotted as a function of the mass number A_1.

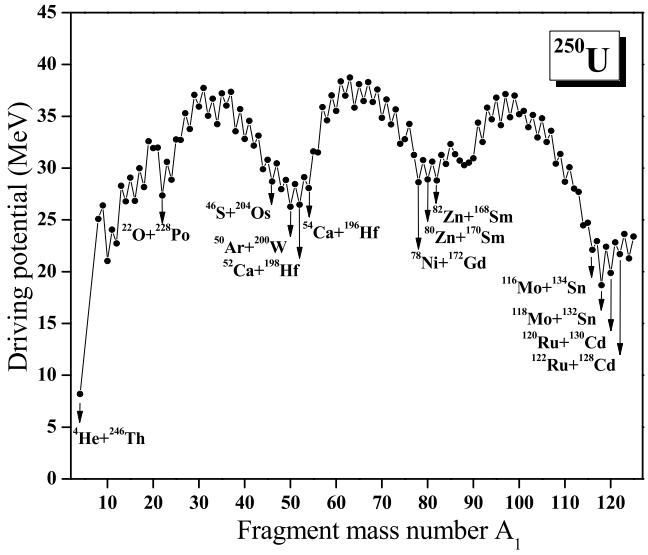

Fig. 6. Driving potential for the ^{250}U isotope, plotted as a function of the mass number A_1.

at doubly-magic ^{132}Sn ($N = 82$, $Z = 50$) is observed for the splitting ^{112}Mo + ^{132}Sn, ^{114}Mo + ^{132}Sn, ^{116}Mo + ^{132}Sn and ^{118}Mo + ^{132}Sn, respectively.

3.2. Barrier penetrability and yield calculation

The barrier penetrability for each fragment combination found in the cold valley for even–even $^{230–250}$U isotopes is calculated using Proximity 1977. The most favorable fragment combinations for all the six isotopes mentioned above are obtained by calculating their relative yields. For a better comparison of barrier penetrability and relative yields, calculations were carried out for all the isotopes using Proximity 2000 as well. Using Eq. (20), the relative yield is calculated and is plotted as a function of the fragment mass numbers A_1 and A_2, as displayed in Figs. 7–17.

For ^{230}U, the combination ^{24}Ne + ^{206}Pb possesses the highest yield due to the presence of a near doubly-magic nucleus ^{206}Pb ($N = 124$, $Z = 82$). The next higher yield is observed for the combination ^{28}Mg + ^{202}Hg, which is due to the near doubly-magic ^{202}Hg ($N = 122$, $Z = 80$) nucleus. The other various peaks in the relative yield graph of Fig. 7 correspond to fragment combinations ^{32}Si + ^{198}Pt, ^{34}Si + ^{196}Pt, ^{94}Sr + ^{136}Xe, ^{96}Zr + ^{134}Te and ^{98}Zr + ^{132}Te. The fragment combination with

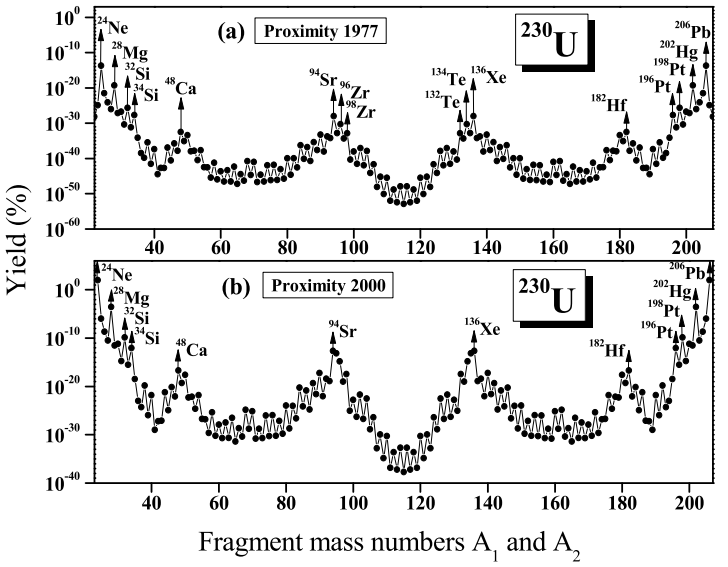

Fig. 7. Relative yield plotted as a function of the mass numbers A_1 and A_2 for the ^{230}U isotope using Proximity 1977 and Proximity 2000. The fragment combinations with higher yields are labeled.

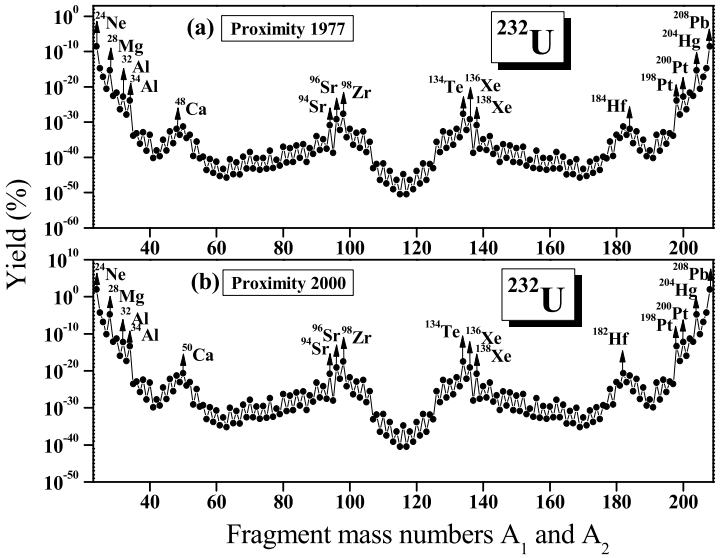

Fig. 8. Relative yield plotted as a function of the mass numbers A_1 and A_2 for the ^{232}U isotope using Proximity 1977 and Proximity 2000. The fragment combinations with higher yields are labeled.

the ^{134}Te and ^{132}Te isotopes are also favored, due to the presence of nearly closed shells ($N = 82$, $Z = 52$) and ($N = 80$, $Z = 52$) respectively.

In the case of the ^{232}U isotope, ^{24}Ne + ^{208}Pb is the most favored binary splitting and it is due to the presence of a doubly-magic nucleus ^{208}Pb ($N = 126$, $Z = 82$). Other favored channels for the binary fission of ^{232}U isotope are ^{28}Mg + ^{204}Hg, ^{32}Si + ^{200}Pt, ^{34}Si + ^{198}Pt, ^{98}Zr + ^{134}Te, and ^{96}Sr + ^{136}Xe, from the most to the less probable one. As can be noticed, these favored channels include the near doubly-magic nucleus ^{204}Hg ($N = 124$, $Z = 80$), neutron shell closure $N = 20$ of ^{34}Si, and the neutron shell closure $N = 82$ of ^{136}Xe and ^{134}Te.

The fragmentation channels that are predicted to be the most favorable ones in the binary fission of ^{234}U isotope are ^{26}Ne + ^{208}Pb, ^{28}Mg + ^{206}Hg, ^{30}Mg + ^{204}Hg, ^{34}Si + ^{200}Pt, ^{100}Zr + ^{134}Te, ^{104}Mo + ^{130}Sn and ^{102}Mo + ^{132}Sn, from the most to the less probable one. One can notice that these channels contain a near doubly-magic ^{206,204}Hg nucleus, doubly-magic nuclei ^{132}Sn ($N = 82$, $Z = 50$) and ^{208}Pb ($N = 126$, $Z = 82$), a neutron shell closure $N = 82$ of ^{134}Te and a proton shell closure $Z = 50$ of ^{130}Sn.

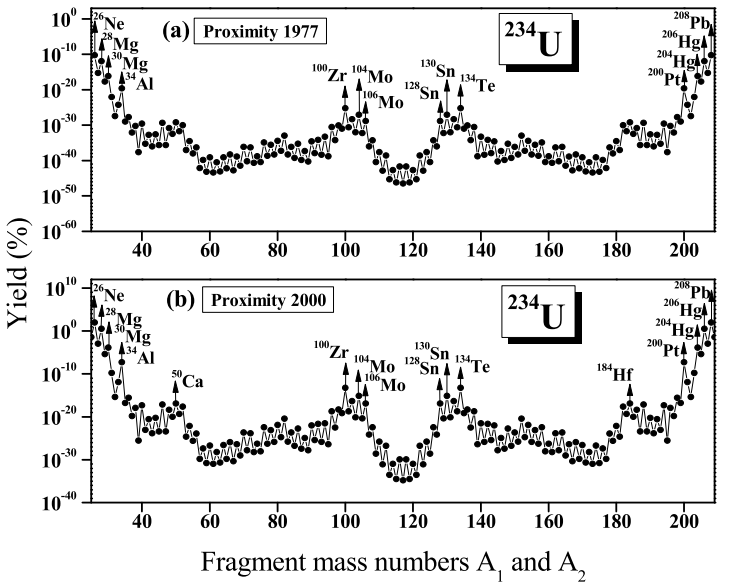

Fig. 9. Relative yield plotted as a function of the mass numbers A_1 and A_2 for the ^{234}U isotope using Proximity 1977 and Proximity 2000. The fragment combinations with higher yields are labeled.

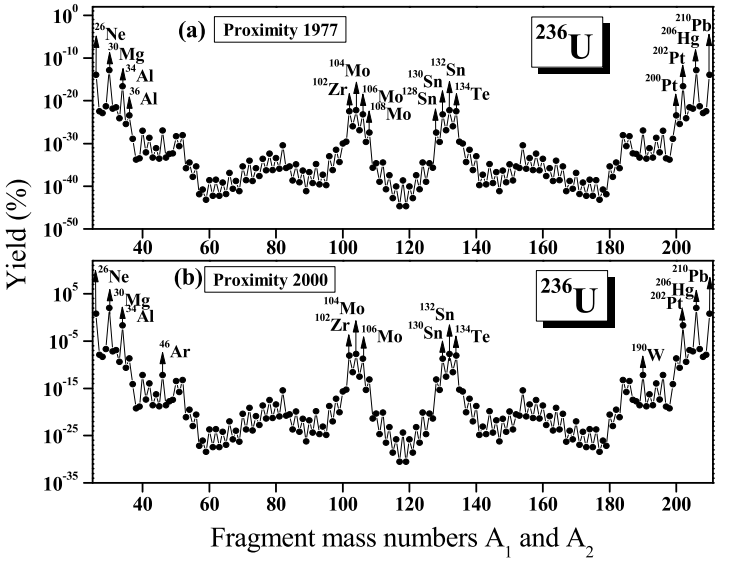

Fig. 10. Relative yield plotted as a function of the mass numbers A_1 and A_2 for the ^{236}U isotope using Proximity 1977 and Proximity 2000. The fragment combinations with higher yields are labeled.

In the case of the ^{236}U isotope, more yield is obtained for the fragment combination ^{30}Mg + ^{206}Hg due to the presence of a near doubly-magic ^{206}Hg ($N = 126$, $Z = 80$) nucleus. The next higher yields are for the fragment splitting ^{26}Ne + ^{210}Pb, ^{34}Si + ^{202}Pt, ^{104}Mo + ^{132}Sn, ^{102}Zr + ^{134}Xe and ^{106}Mo + ^{130}Sn. It is due to the near doubly-magic ^{210}Pb ($N = 128$, $Z = 82$) nucleus, the magic neutron shell $N = 20$ of ^{34}Si, the doubly-magic nucleus ^{132}Sn ($N = 82$, $Z = 50$) and the near doubly-magic ^{130}Sn nucleus.

For the ^{238}U isotope, the highest yield is obtained for the fragment combination ^{34}Si + ^{204}Pt due to the magic neutron shell $N = 126$ of ^{204}Pt. The next higher yields are for the fragment combinations ^{30}Mg + ^{208}Hg, ^{32}Mg + ^{206}Hg, ^{106}Mo + ^{132}Sn, ^{36}Si + ^{202}Pt, and ^{108}Mo + ^{130}Sn. The occurrence of these fragment combinations are attributed to the presence of the near doubly-magic ^{130}Sn ($N = 80$, $Z = 50$), ^{208}Hg ($N = 128$, $Z = 80$), ^{206}Hg ($N = 126$, $Z = 80$), ^{134}Te ($N = 82$, $Z = 52$) and doubly-magic ^{132}Sn ($N = 82$, $Z = 50$) nuclei.

From Fig. 12, it is clear that, for the ^{240}U isotope, the highest yield is obtained for the symmetric fragment combination ^{108}Mo + ^{132}Sn as it contains a doubly-magic nucleus ^{132}Sn ($N = 82$, $Z = 50$). The next higher yields are for the fragment combinations ^{36}Si + ^{204}Pt, ^{110}Mo + ^{130}Sn, ^{42}S + ^{198}Os, ^{40}S + ^{200}Os, ^{46}Ar + ^{194}W and ^{50}Ca + ^{190}Hf. It is due to the

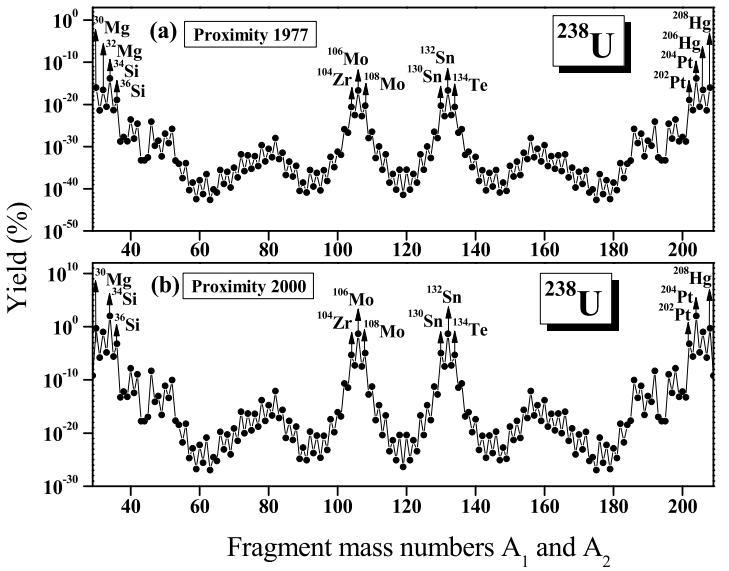

Fig. 11. Relative yield plotted as a function of the mass numbers A_1 and A_2 for the ^{238}U isotope using Proximity 1977 and Proximity 2000. The fragment combinations with higher yields are labeled.

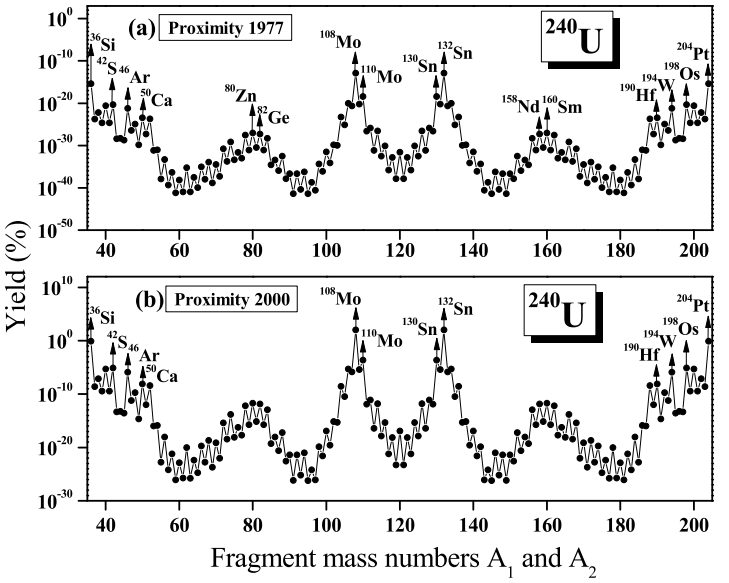

Fig. 12. Relative yield plotted as a function of the mass numbers A_1 and A_2 for the ^{240}U isotope using Proximity 1977 and Proximity 2000. The fragment combinations with higher yields are labeled.

presence of the magic neutron shell $N = 126$ of ^{204}Pt, of the near doubly-magic nucleus ^{130}Sn, of the near neutron shell closure $N = 124$ of ^{200}Os, of the neutron shell closure $N = 28$ of ^{46}Ar, and of the magic shell $Z = 20$ of ^{50}Ca.

For the ^{242}U isotope, the highest maximum of the yield belongs to the fragment combination ^{110}Mo + ^{132}Sn that contains a doubly-magic nucleus ^{132}Sn ($N = 82$, $Z = 50$). The other various peaks correspond to the fragment combinations ^{42}S + ^{200}Os, ^{46}Ar + ^{196}W, ^{112}Mo + ^{130}Sn, ^{52}Ca + ^{190}Hf and ^{106}Zr + ^{136}Te. The occurrence of these fragment combinations is attributed to the presence of the near neutron shell closure $N = 124$ of ^{200}Os, of the near doubly-magic ^{46}Ar, ^{130}Sn, ^{136}Te nuclei, and of the magic shell $Z = 20$ of ^{52}Ca.

In the case of the ^{244}U isotope, the highest yield is for the symmetric fragment combination ^{112}Mo + ^{132}Sn. The next higher yields are for the fragment combinations ^{42}S + ^{202}Os, ^{46}Ar + ^{198}W, ^{48}Ar + ^{196}W and ^{52}Ca + ^{192}Hf. This is due to the presence of the neutron shell closures $N = 126$ of ^{202}Os and $N = 28$ of ^{46}Ar, and of the magic shell $Z = 20$ of ^{52}Ca.

For the ^{246}U isotope, the highest yield is obtained for the fragment combination ^{114}Mo + ^{132}Sn. The next higher yields are for the fragment combinations ^{46}Ar + ^{200}W, ^{48}Ar + ^{198}W, ^{116}Ru + ^{130}Cd, and ^{52}Ca + ^{194}Hf. It was found that the first

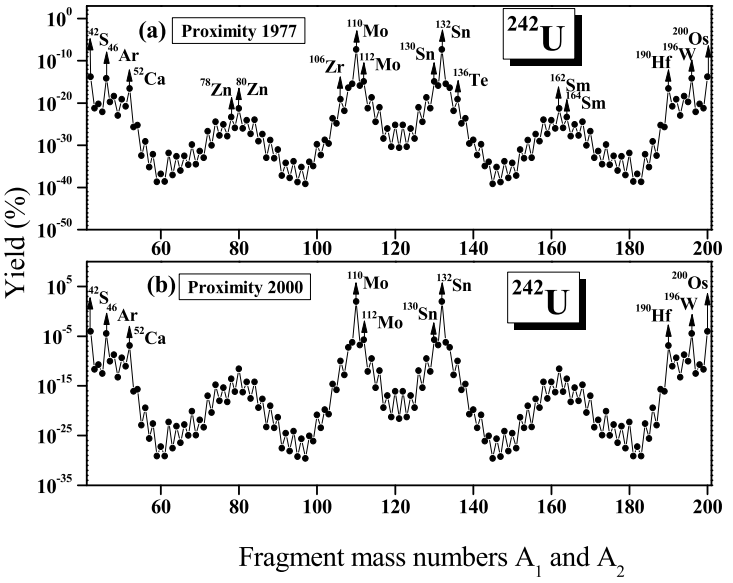

Fig. 13. Relative yield plotted as a function of the mass numbers A_1 and A_2 for the ^{242}U isotope using Proximity 1977 and Proximity 2000. The fragment combinations with higher yields are labeled.

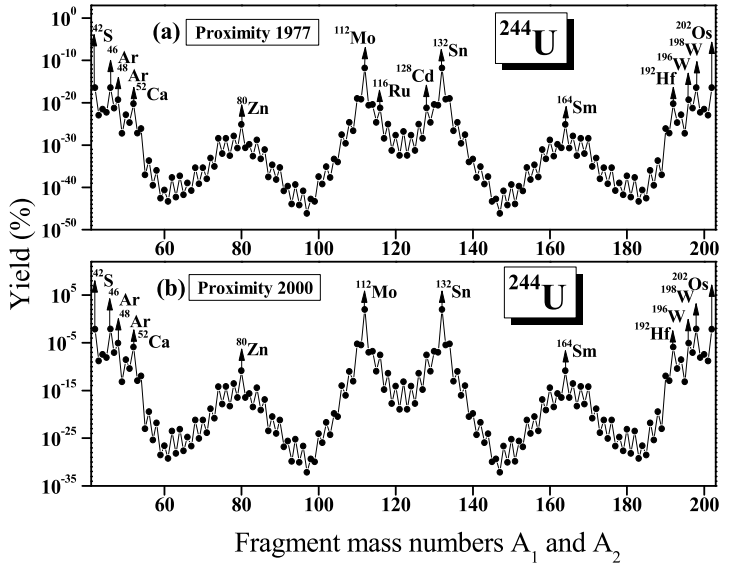

Fig. 14. Relative yield plotted as a function of the mass numbers A_1 and A_2 for the ^{244}U isotope using Proximity 1977 and Proximity 2000. The fragment combinations with higher yields are labeled.

one is attributed to the magic neutron $N = 28$ of ^{46}Ar and $N = 126$ of ^{200}W, and the second combination is due to the near doubly closed shell ($N = 30$, $Z = 18$) of the ^{48}Ar nucleus. The fragment combination with the ^{130}Cd isotope is also favored due to the presence of a nearly magic shell ($N = 82$, $Z = 48$).

For the ^{248}U isotope, the highest yield is obtained for the fragment combination ^{116}Mo + ^{132}Sn. The next higher yields are for the fragment combinations ^{48}Ar + ^{200}W, ^{118}Ru + ^{130}Cd, ^{52}Ca + ^{196}Hf, and ^{114}Mo + ^{134}Sn. The fragment combination with the ^{134}Sn isotope is also favored due to the presence of a nearly closed shell ($N = 84$, $Z = 50$).

For ^{250}U isotope, the highest yield is obtained for the fragment combination ^{118}Mo + ^{132}Sn. The next higher yields are for the fragment combinations ^{120}Ru + ^{130}Cd, ^{52}Ca + ^{198}Hf, ^{50}Ar + ^{200}W, ^{116}Mo + ^{134}Sn, and ^{48}Ar + ^{202}W. The fragment combination with the ^{198}Hf isotope is also favored due to the presence of the magic neutron $N = 126$.

From Figs. 7–17, it becomes clear that, for all the chosen uranium isotopes, the highest yield is obtained for the same fragment combination when using the potentials Proximity 1977 and Proximity 2000. Moreover, the ordering of other fragment combinations from the most probable to the least probable one was also the same for both potentials.

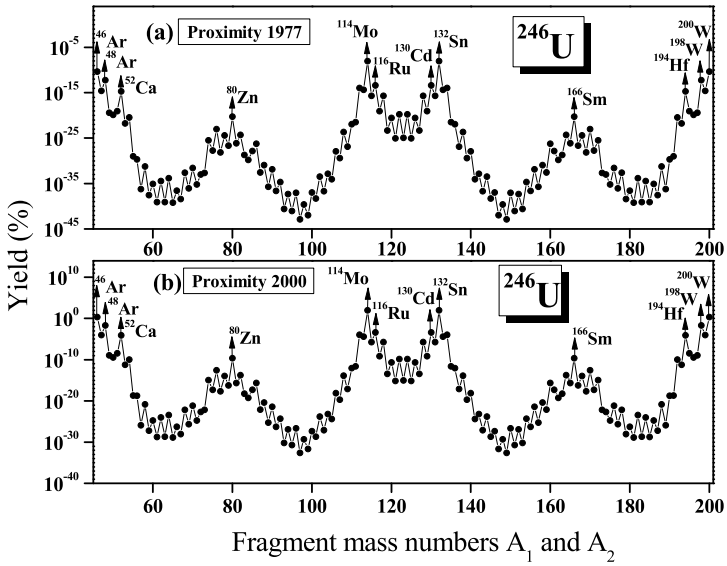

Fig. 15. Relative yield plotted as a function of the mass numbers A_1 and A_2 for the ^{246}U isotope using Proximity 1977 and Proximity 2000. The fragment combinations with higher yields are labeled.

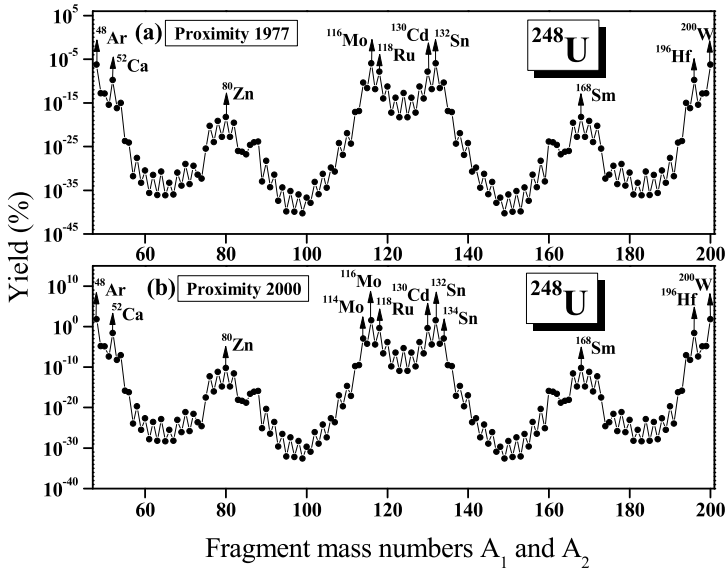

Fig. 16. Relative yield plotted as a function of the mass numbers A_1 and A_2 for the ^{248}U isotope using Proximity 1977 and Proximity 2000. The fragment combinations with higher yields are labeled.

We have computed the half-lives for the binary splitting of the ^{232,234,236,238}U isotopes using Proximity 1977 and Proximity 2000, making use of the relation

$$T_{1/2} = \left(\frac{\ln 2}{\nu P}\right) \tag{21}$$

where ν is the assault frequency and P is the barrier penetrability.

The computed half-life values have been compared with available experimental values [47] and are presented in Table 1. The average deviation is found to be less than 10^2 times between the theoretical and experimental spontaneous fission half-life values. This level of agreement is very satisfactory since spontaneous fission is a much more complex process than α decay.

We have extracted the values of experimental penetrability from Holden et al. [47] and compared them with the theoretical values of penetrability. The results are shown in Table 1. From the tabulated results, it is clear that the experimental penetrability for ^{236}U was reproduced with the same order.

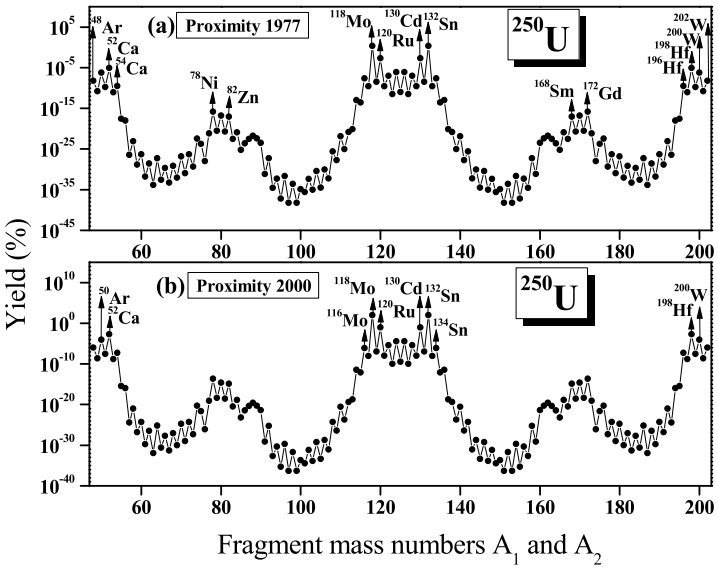

Fig. 17. Relative yield plotted as a function of the mass numbers A_1 and A_2 for the ^{250}U isotope using Proximity 1977 and Proximity 2000. The fragment combinations with higher yields are labeled.

Table 1
Comparison of the calculated penetrability and calculated half-lives of U isotopes in the range $232 \leq A \leq 238$ using Proximity 1977 and Proximity 2000 with the experimental values [47].

Parent nucleus	Decay channel	Penetrability			$T_{1/2}$ (s)		
		1977	2000	Exp	1977	2000	Exp
^{232}U	^{98}Zr + ^{134}Te	8.17E−45	2.77E−46	2.82E−42	8.48E+23	2.51E+25	2.45E+21
^{234}U	^{100}Zr + ^{134}Te	6.72E−46	1.70E−47	1.48E−44	1.03E+25	4.07E+26	4.67E+23
^{236}U	^{102}Zr + ^{134}Te	3.53E−45	7.19E−47	8.93E−45	1.96E+24	9.64E+25	7.76E+23
^{238}U	^{106}Mo + ^{132}Sn	9.74E−42	1.93E−43	2.69E−44	7.11E+20	3.59E+22	2.57E+23

4. Conclusions

To study the binary fragmentation of even–even $^{230–250}$U isotopes, the Coulomb and the proximity potential are taken as the interacting barrier. In each case, the fragmentation potential and Q-values were calculated for all the possible fission components. The relative yields were calculated using Proximity 1977 and Proximity 2000. It can be seen that as the mass number of the parent nuclei increases, the magnitude of the relative yield also increases. The predicted favorable fragment combinations for the binary fission of all the chosen uranium isotopes have been discussed in detail in Section 3.2. For the ^{230,232,234}U isotopes, the highest yield was predicted for the isotope of Pb ($Z = 82$) as one fragment, whereas for the ^{236}U isotope fragments with the isotope of Hg ($Z = 80$) as one fragment possess the highest yield. For the ^{238}U isotope, fragments with the isotope of Pt ($Z = 78$, $N = 126$) as one fragment possess the highest yield. In the case of the ^{240,242,244,246,248,250}U isotopes, the highest yield is for the fragments with Sn ($Z = 50$) as one fragment. The double magicity and near double magicity of the predicted heavy fragment (of ^{206,208}Pb, ^{206}Hg, ^{204}Pt, ^{200,202}Os and ^{130,132}Sn) are found to play a key role for the most favorable fragment combinations. The computed penetrability and half-lives using the two different proximity potentials for the binary fission of ^{230,234,236,238}U agrees with the experimental values of Holden et al. [47] (Table 1).

Acknowledgements

One of the authors (KPS) would like to thank the University Grants Commission, Government of India for the financial support under Major Research Project No. 42-760/2013 (SR) dated 22-03-2013.

References

[1] O. Hahn, F. Strassmann, Naturwissenschaften 27 (1939) 11.
[2] N. Bohr, J.A. Wheeler, Phys. Rev. 56 (1939) 426.
[3] J.C.D. Milton, J.S. Fraser, Can. J. Phys. 40 (1962) 1626.
[4] F. Gonnenwein, B. Borsig, Nucl. Phys. A 530 (1991) 27.
[5] A. Sandulescu, A. Florescu, W. Greiner, J. Phys. G, Nucl. Part. Phys. 15 (1989) 1815.
[6] C. Guet, M. Ashgar, P. Perrin, C. Signarbieux, Nucl. Instrum. Methods 150 (1978) 189.

[7] F.J. Hambsch, H.H. Knitter, C. Budtz-Jorgensen, Nucl. Phys. A 554 (1993) 209.
[8] A. Benoufella, G. Barreau, M. Asghar, P. Audouard, F. Brisard, T.P. Doan, M. Hussonnois, B. Leroux, J. Trochon, M.S. Moore, Nucl. Phys. A 565 (1993) 563.
[9] W. Schwab, H.G. Clerc, M. Mutterer, J.P. Theobald, H. Faust, Nucl. Phys. A 577 (1994) 674.
[10] J.H. Hamilton, A.V. Ramayya, J. Kormicki, W.C. Ma, Q. Lu, D. Shi, J.K. Deng, S.J. Zhu, A. Sandulescu, W. Greiner, G.M. Ter-Akopian, Y.Ts. Oganessian, G.S. Popeko, A.V. Daniel, J. Kliman, V. Polhorsky, M. Morhac, J.D. Cole, R. Aryaeinejad, I.Y. Lee, N.R. Johnson, F.K. McGowan, J. Phys. G, Nucl. Part. Phys. 20 (1994) L85.
[11] G.M. Ter-Akopian, J.H. Hamilton, Y.Ts. Oganessian, J. Kormicki, G.S. Popeko, A.V. Daniel, A.V. Ramayya, Q. Lu, K. Butler-Moore, W.C. Ma, J.K. Deng, D. Shi, J. Kliman, V. Polhorsky, M. Morhac, W. Greiner, A. Sandulescu, J.D. Cole, R. Aryaeinejad, N.R. Johnson, I.Y. Lee, F.K. McGowan, Phys. Rev. Lett. 73 (1994) 1477.
[12] A. Sandulescu, A. Florescu, F. Carstoiu, W. Greiner, J.H. Hamilton, A.V. Ramayya, B.R.S. Babu, Phys. Rev. C 54 (1996) 258.
[13] A. Sandulescu, S. Misicu, F. Carstoiu, A. Florescu, W. Greiner, Phys. Rev. C 57 (1998) 2321.
[14] M. Montoya, arXiv:1410.1238v1 [nucl-ex], 2014.
[15] M. Asghar, N. Boucheneb, G. Medkour, P. Geltenbort, B. Leroux, Nucl. Phys. A 560 (1993) 677.
[16] P.G. Reinhard, M. Bender, K. Rutz, J.A. Maruhn, Z. Phys. A 358 (1997) 277.
[17] M. Girod, P. Schuck, Phys. Rev. Lett. 111 (2013) 132503.
[18] P. Ring, P. Schuck, The Nuclear Many-Body Problem, Springer Verlag, Berlin, 1980.
[19] S. Goriely, S. Hilaire, M. Girod, S. Peru, Phys. Rev. Lett. 102 (2009) 242501.
[20] J-F. Berger, M. Girod, D. Gogny, Nucl. Phys. A 428 (1984) 23c.
[21] F. Chappert, M. Girod, S. Hilaire, Phys. Lett. B 668 (2008) 420.
[22] J. Decharge, D. Gogny, Phys. Rev. C 21 (1980) 1568.
[23] R. Rodriguez-Guzman, L.M. Robledo, Phys. Rev. C 89 (2014) 054310.
[24] Y.J. Shi, W.J. Swiatecki, Nucl. Phys. A 438 (1985) 450.
[25] S.S. Malik, R.K. Gupta, Phys. Rev. C 39 (1989) 1992.
[26] W.D. Myers, W.J. Swiatecki, Phys. Rev. C 62 (2000) 044610.
[27] W. Reisdorf, J. Phys. G, Nucl. Part. Phys. 20 (1994) 1297.
[28] I. Dutt, R.K. Puri, Phys. Rev. C 81 (2010) 064608.
[29] I. Dutt, R.K. Puri, Phys. Rev. C 81 (2010) 064609.
[30] I. Dutt, Pramana J. Phys. 76 (2011) 921.
[31] Y.J. Yao, G.L. Zhang, W.W. Qu, J.Q. Qian, Eur. Phys. J. A 51 (2015) 122.
[32] K.P. Santhosh, S. Sahadevan, R.K. Biju, Nucl. Phys. A 825 (2009) 159.
[33] K.P. Santhosh, B. Priyanka, Eur. Phys. J. A 49 (2013) 150.
[34] K.P. Santhosh, B. Priyanka, Int. J. Mod. Phys. E 22 (2013) 1350081.
[35] S. Peltonen, Ph.D. Thesis, University of Jyvaskyla, Finland, 2009.
[36] K.P. Santhosh, A. Joseph, Pramana J. Phys. 59 (2002) 599.
[37] K.P. Santhosh, R.K. Biju, S. Sahadevan, A. Joseph, Phys. Scr. 77 (2008) 065201.
[38] K.P. Santhosh, R.K. Biju, A. Joseph, J. Phys. G, Nucl. Part. Phys. 35 (2008) 085102.
[39] K.P. Santhosh, B. Priyanka, Nucl. Phys. A 929 (2014) 20.
[40] K.P. Santhosh, S. Krishnan, Eur. Phys. J. A 52 (2016) 108.
[41] K.P. Santhosh, S. Krishnanand, B. Priyanka, J. Phys. G, Nucl. Part. Phys. 41 (2014) 105108.
[42] K.P. Santhosh, S. Krishnanand, B. Priyanka, Phys. Rev. C 91 (2015) 044603.
[43] K.P. Santhosh, R.K. Biju, S. Sahadevan, J. Phys. G, Nucl. Part. Phys. 36 (2009) 115101.
[44] K.P. Santhosh, R.K. Biju, J. Phys. G, Nucl. Part. Phys. 36 (2009) 015107.
[45] K.P. Santhosh, R.K. Biju, S. Sahadevan, Nucl. Phys. A 832 (2010) 220.
[46] A. Cyriac, K.P. Santhosh, IOSR J. Appl. Phys. 1 (2017) 86.
[47] N.E. Holden, D.C. Hoffman, Pure Appl. Chem. 72 (2000) 1525.
[48] K.P. Santhosh, A. Cyriac, S. Krishnan, Nucl. Phys. A 949 (2016) 8.
[49] K.P. Santhosh, A. Cyriac, S. Krishnan, Indian J. Phys. 92 (2018) 1589.
[50] J. Blocki, J. Randrup, W.J. Swiatecki, C.F. Tsang, Ann. Phys. 105 (1977) 427.
[51] J. Blocki, W.J. Swiatecki, Ann. Phys. 132 (1981) 53.
[52] W.D. Myers, W.J. Swiatecki, Ann. Phys. 84 (1969) 186;
W.D. Myers, W.J. Swiatecki, Nucl. Phys. A 336 (1980) 267.
[53] B. Nerlo-Pomorska, K. Pomorski, Z. Phys. A 348 (1994) 169.
[54] M. Wang, G. Audi, F.G. Kondev, W.J. Huang, S. Naimi, X. Xu, Chin. Phys. C 41 (2017) 030003.
[55] H. Koura, T. Tachibana, M. Uno, M. Yamada, Prog. Theor. Phys. 113 (2005) 305.